Electronic Supplementary Material (ESI) for Journal of Materials Chemistry A.

Supporting Information

Insight on Charge Transport Correlation in Au_x Clusters and Graphene Quantum Dots Deposited on TiO_2 Nanotubes for Photoelectrochemical Oxygen Evolution

Zhiping Zeng,[a,b] Yu-Bing Li,[a] Shufen Chen,[b] Peng Chen,[b] Fang-Xing Xiao[a]*

College of Materials Science and Engineering, Fuzhou University, Fuzhou 350108, China.

E-mail: *fxxiao@fzu.edu.cn*

School of Chemical and Biomedical Engineering, Nanyang Technological University, Singapore 639798, Singapore.

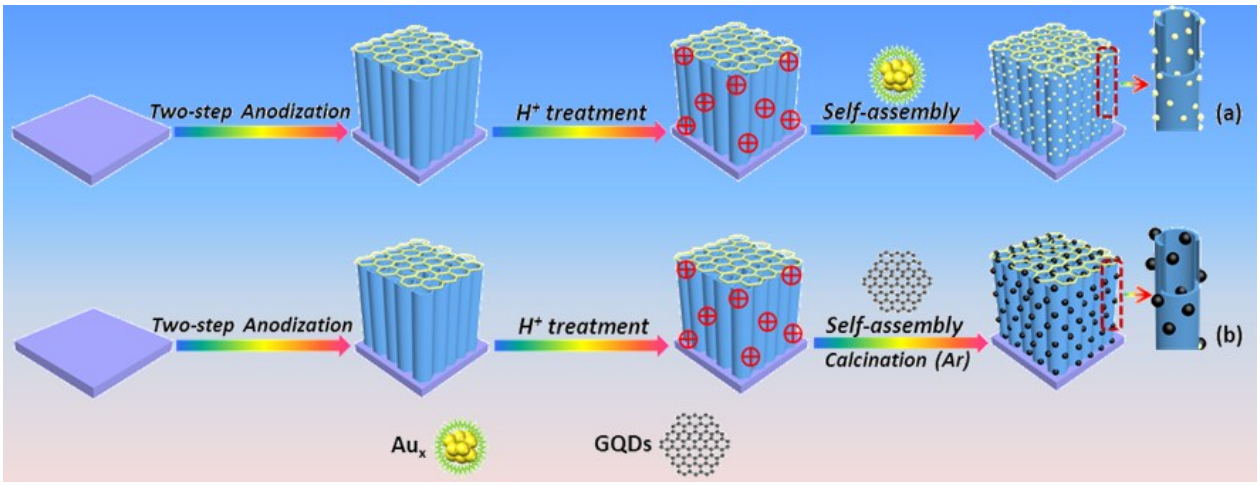

Fig. S1 Schematic illustration for fabrication of (a) Au_x/NP-TNTAs and (b) GQDs/NP-TNTAs binary heterostructures via direct electrostatic self-assembly strategy.

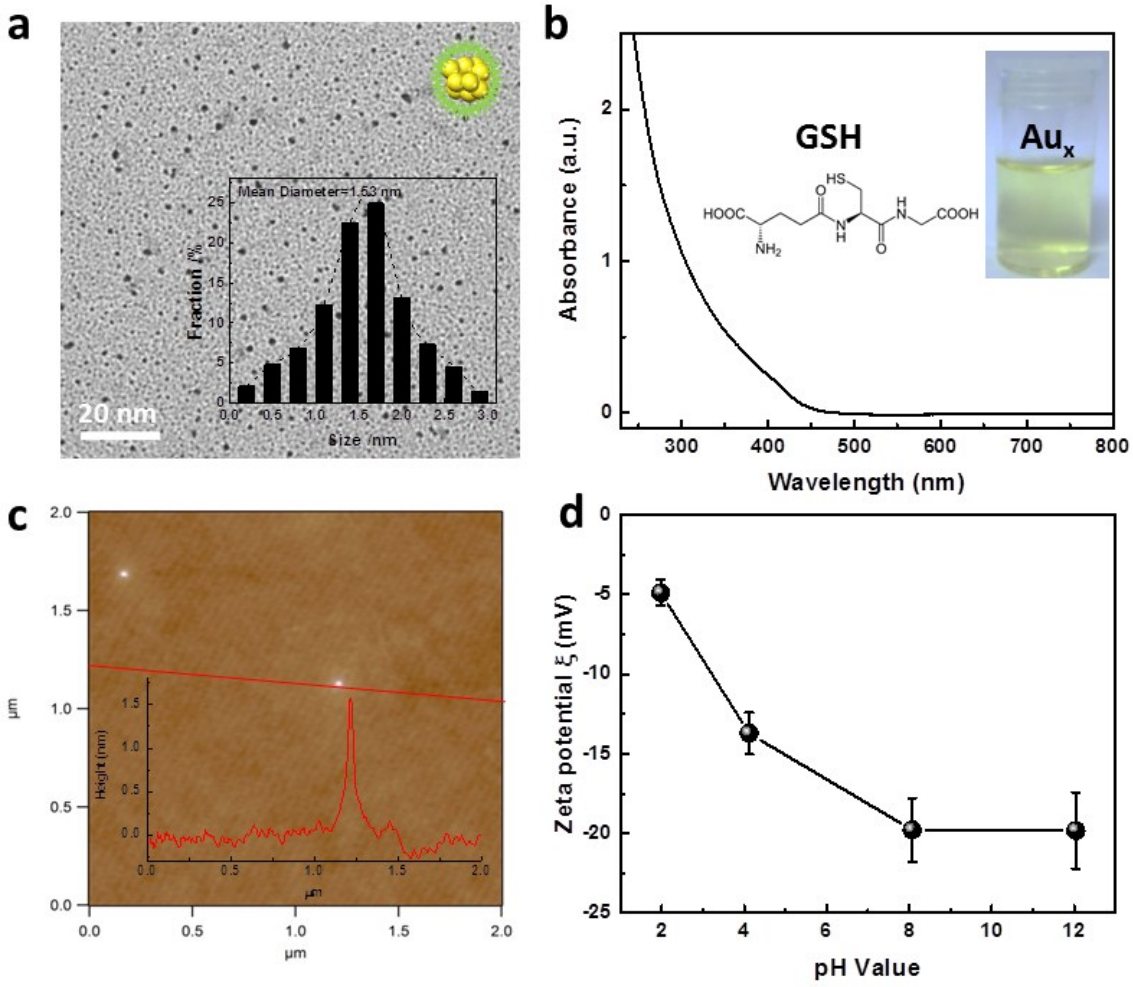

Fig. S2 (a) TEM image of GSH-capped Au_x clusters with corresponding size distribution histogram in the inset, (b) UV-vis absorption spectrum of Au_x clusters aqueous solution, (c) AFM image of Au_x clusters with corresponding height profile in the inset, and (d) zeta potential of Au_x clusters as a function of pH value. Schematic model of Au_x clusters and molecular structure of GSH were provided in the insets of a and b.

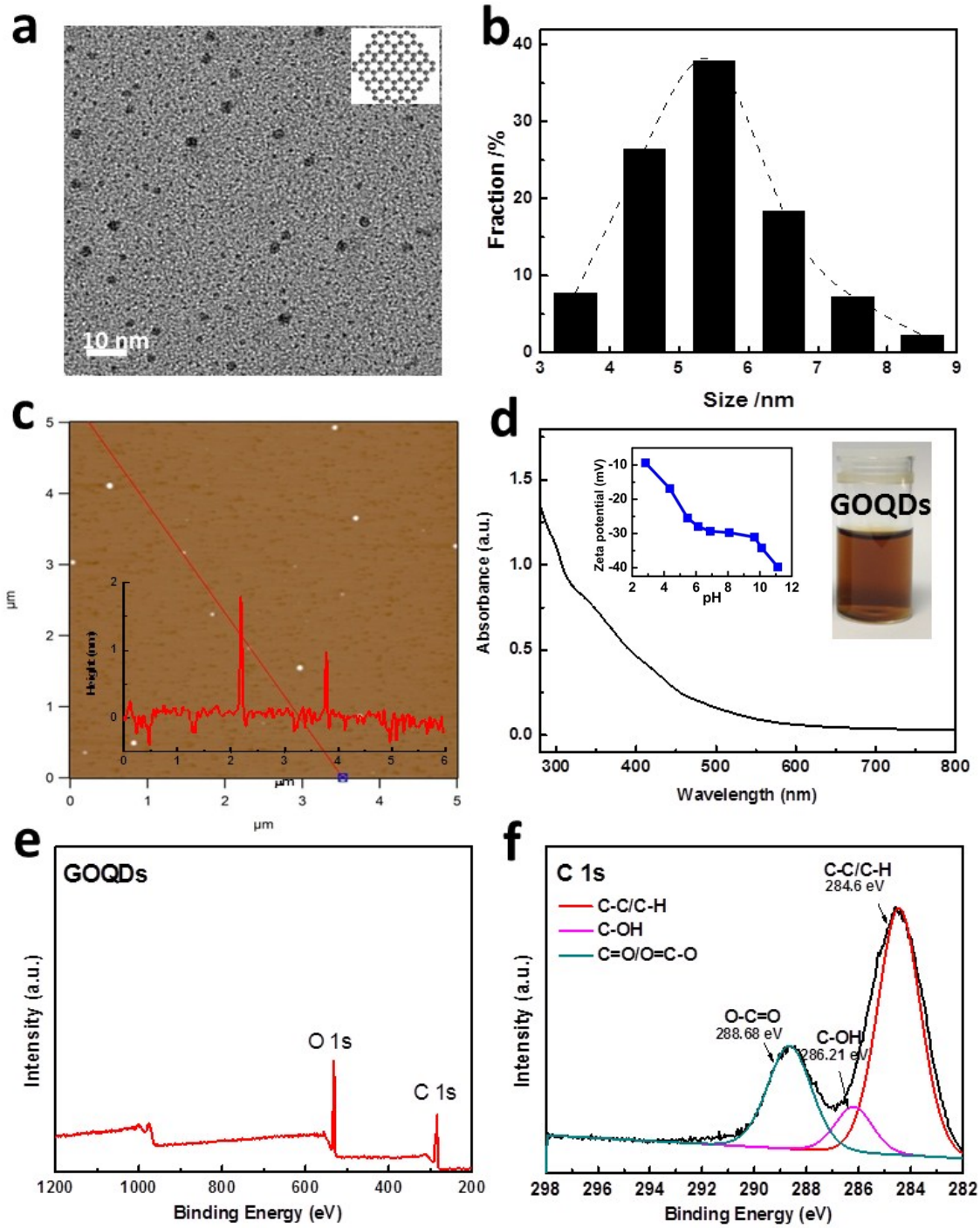

Fig. S3 (a) TEM image of GOQDs with corresponding (b) size distribution histogram, (c) AFM image of GOQDs with corresponding height profile in the inset, (d) UV-vis absorption spectrum of GOQDs aqueous solution with corresponding photograph in the inset, and (e) survey and (f) high-resolution C 1s XPS spectra of GOQDs. Schematic model of GOQDs and its Zeta potential as a function of pH was provided in the insets of a and d, respectively.

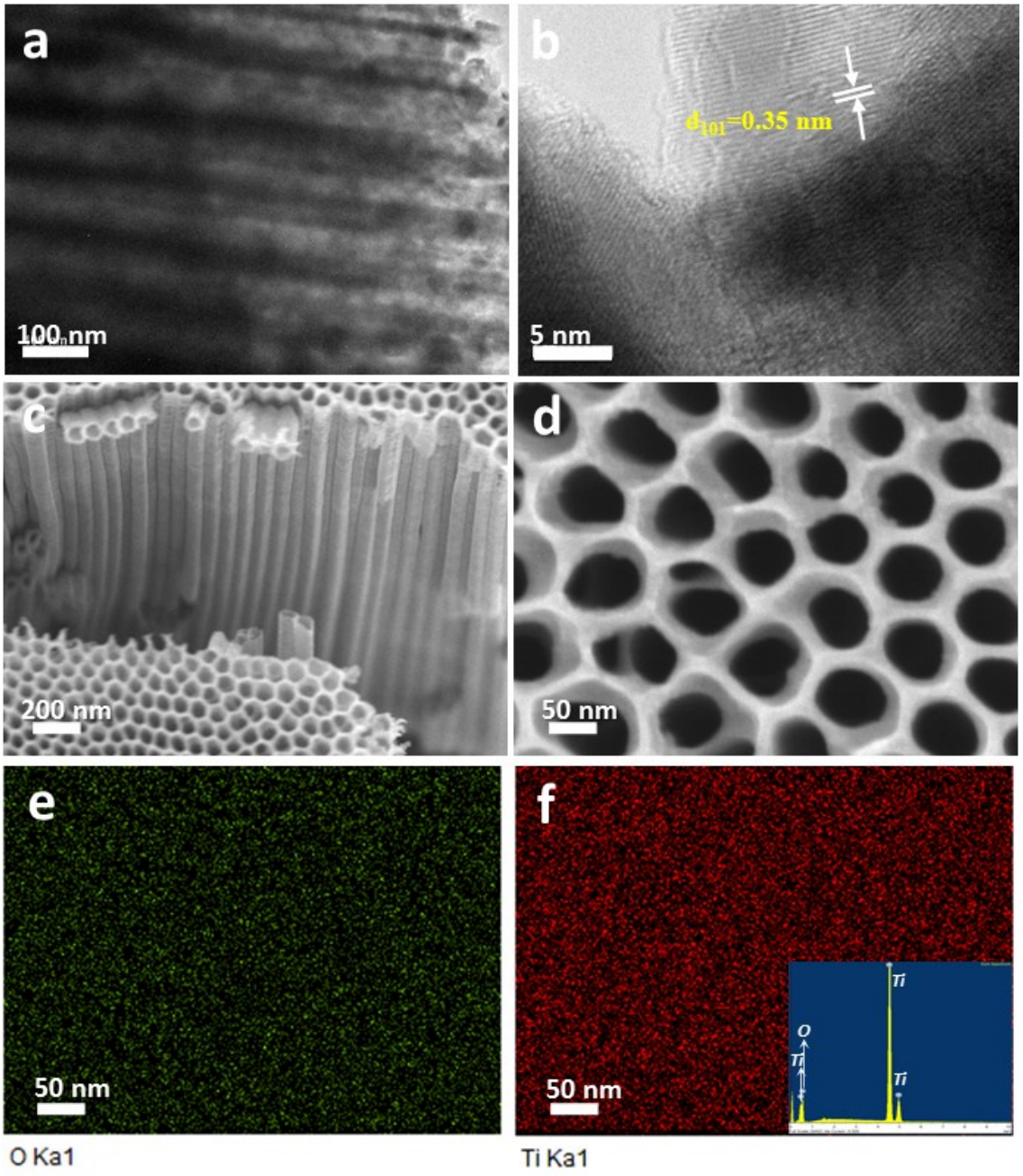

Fig. S4 (a) TEM, (b) HRTEM, (c) cross-sectional and (d) panoramic FESEM images of pristine NP-TNTAs substrate with corresponding (e & f) element mapping and EDS results (inset).

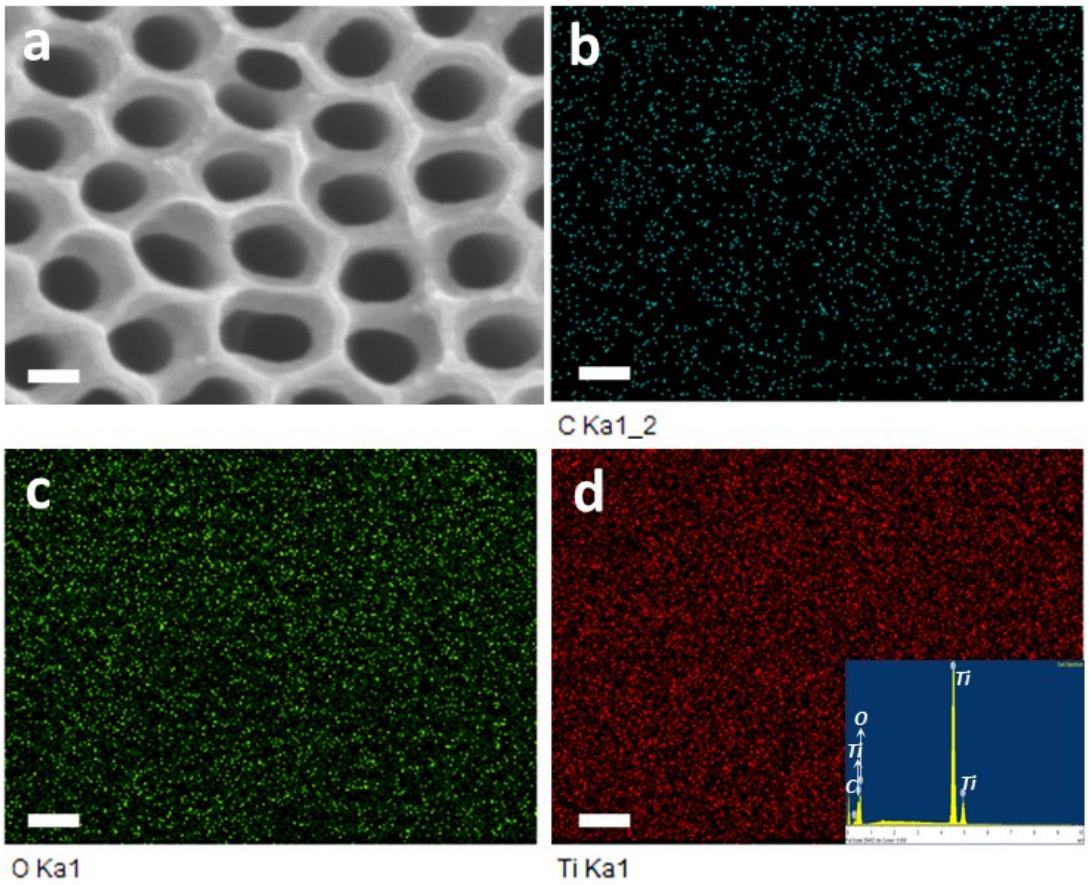

Fig. S5 (a) FESEM image and elemental mapping (b-d) results of GQDs/NP-TNTAs binary heterostructure with corresponding EDS pattern in the inset of d.

Note: Carbon signal arising from GQDs were clearly observed on the whole scaffold of NP-TNTAs, indicative of efficacious self-assembly of GQDs on the NP-TNTAs substrate via electrostatic interaction.

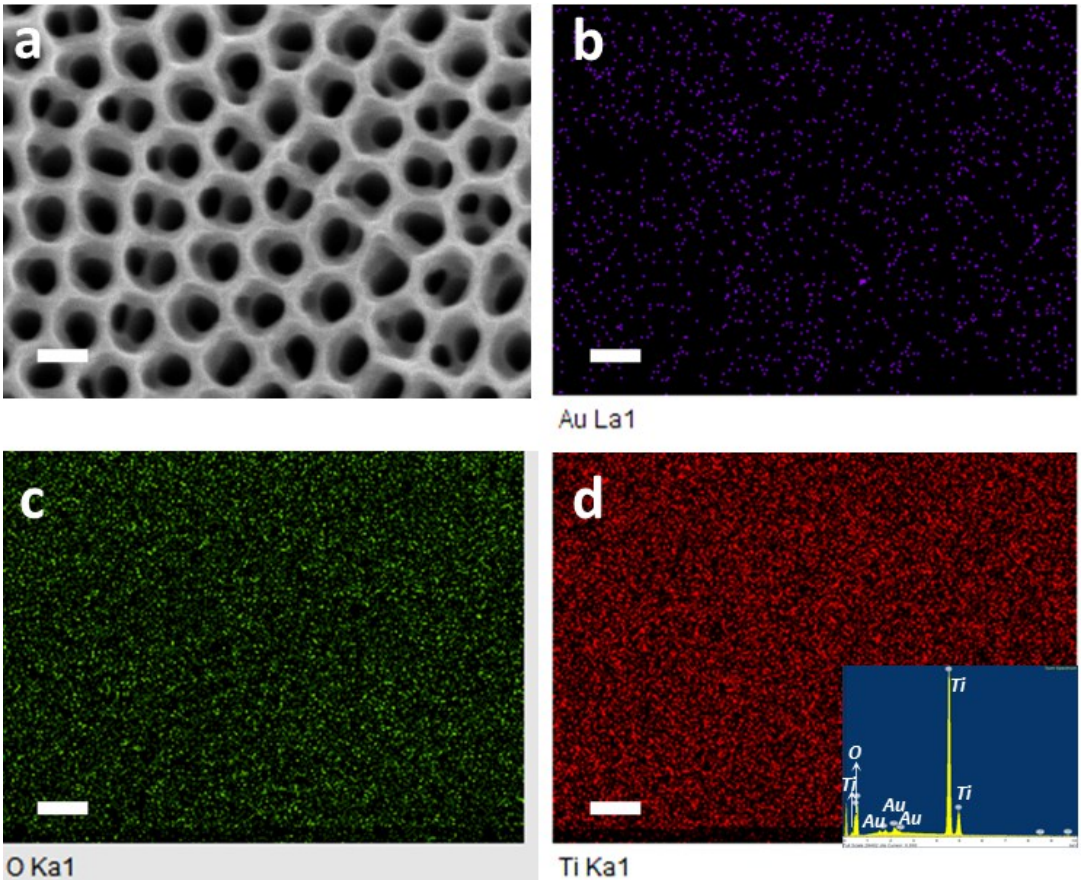

Fig. S6 (a) FESEM image and (b-d) elemental mapping results of Au_x/NP-TNTAs binary heterostructure with corresponding EDS pattern in the inset.

Note: It is apparent that Au signal was uniformly distributed on the whole framework of NP-TNTAs, strongly evidencing Au_x clusters have been anchored on the NP-TNTAs substrate via electrostatic interaction.

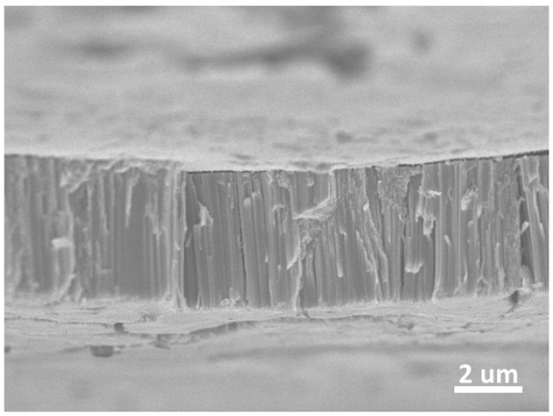

Fig. S7 Cross-sectional FESEM image of Au_x/GQDs/NP-TNTAs ternary heterostructure.

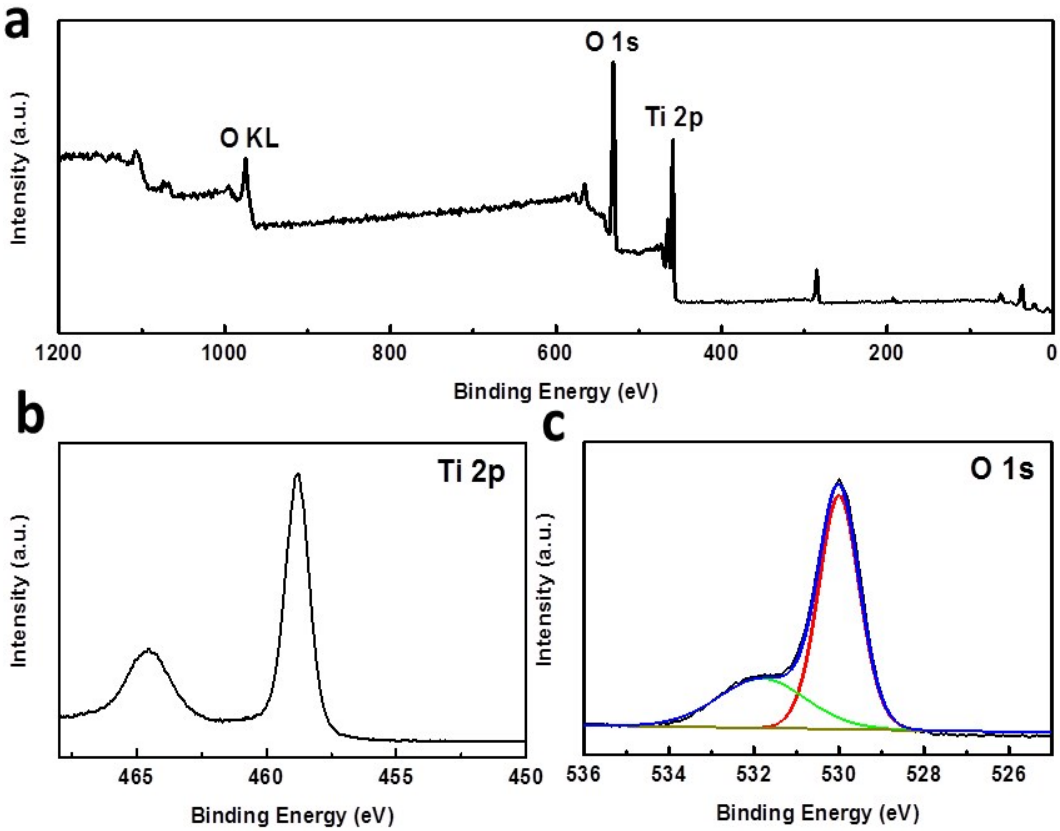

Fig. S8 (a) Survey spectrum and high-resolution XPS spectra of (b) Ti 2p and (c) O 1s for pristine NP-TNTAs substrate.

Table S1. Binding energy vs chemical bond species for pristine NP-TNTAs substrate.

Element	***NP-TNTAs substrate (eV)***	***Chemical Bond Species***
Ti $2p_{3/2}$	458.82	Ti-O
Ti $2p_{1/2}$	464.56	Ti-O
O 1s A	530.03	Lattice oxygen (Ti-O)
O 1s B	531.85	Surface hydroxyl (Ti-OH)

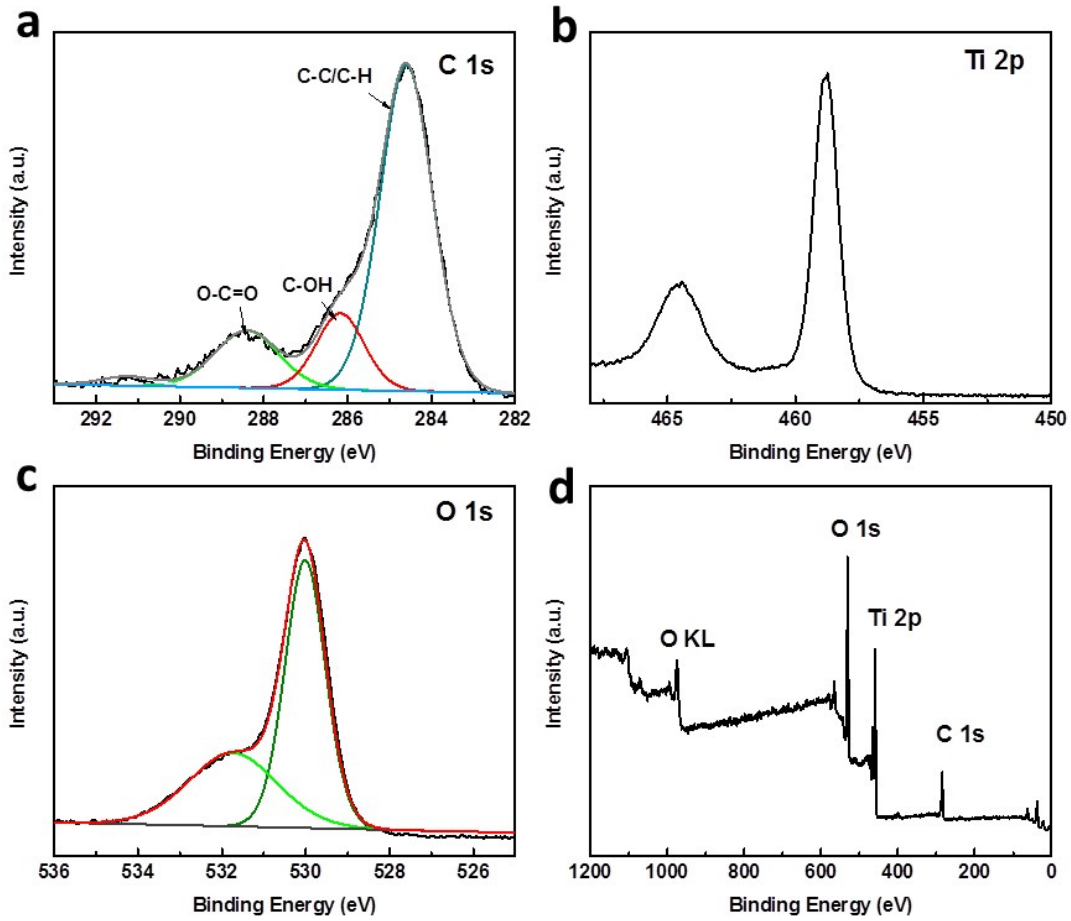

Fig. S9 High-resolution XPS spectra of (a) C 1s, (b) Ti 2p, and (c) O 1s along with (d) survey spectrum for GQDs/NP-TNTAs binary heterostructure.

Note: High-resolution C 1s spectrum of GQDs/NP-TNTAs binary heterostructure is similar to pristine GQDs, indicative of successful assembly of GQDs on the NP-TNTAs framework via electrostatic attractive interaction. High-resolution Ti 2p spectrum corresponds to Ti^{4+} which suggests intact crystal structure of TiO_2 substrate.

Table S2. Binding energy *vs* chemical bond species for GQDs/NP-TNTAs binary heterostructure.

Element	***Au_x/NP-TNTAs (eV)***	***Chemical Bond Species***
Ti $2p_{3/2}$	458.83	Ti-O
Ti $2p_{1/2}$	464.52	Ti-O
O 1s A	530.03	Lattice oxygen (Ti-O)
O 1s B	531.73	Surface hydroxyl (Ti-OH)
C 1s A	284.60	C-C/C-H
C 1s B	286.19	C-OH/C-O-C
C 1s C	288.41	O-C=O

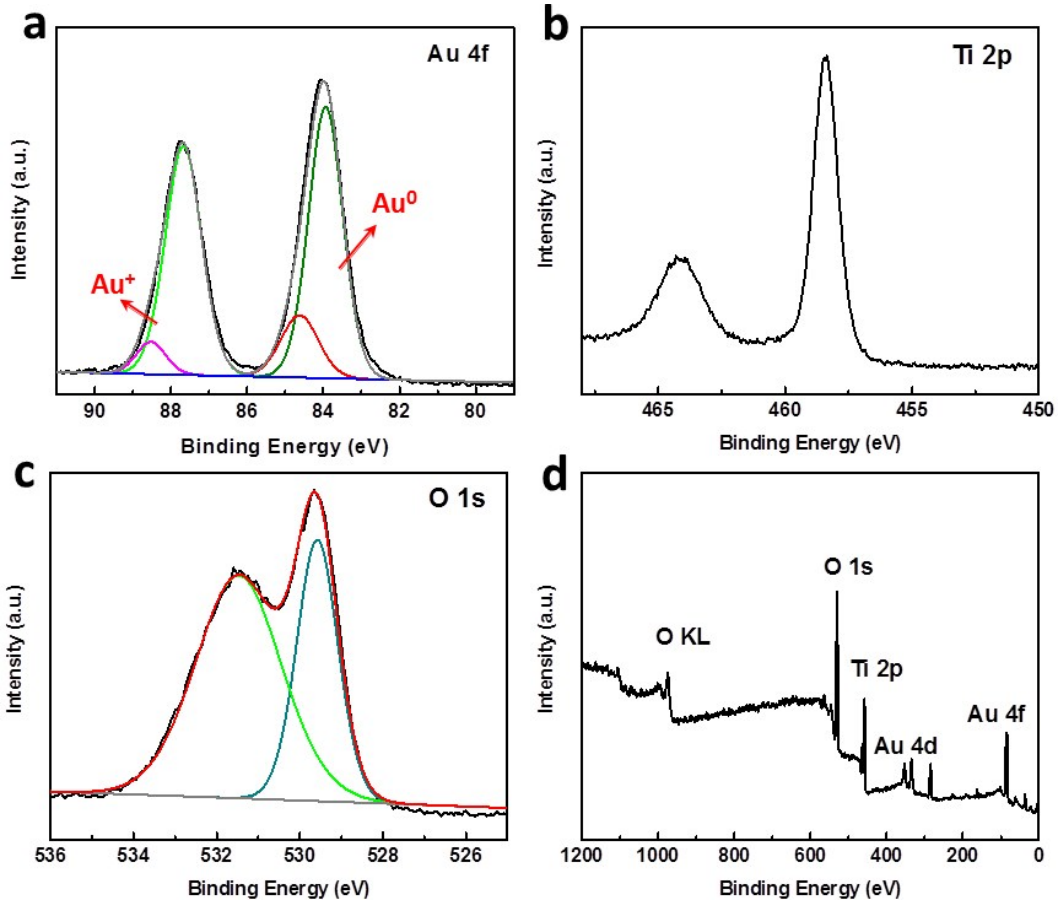

Fig. S10 High-resolution XPS spectra of (a) Au 4f, (b) Ti 2p, and (c) O 1s together with (d) survey spectrum for Au_x/NP-TNTAs binary heterostructure.

Note: High-resolution Au 4f spectrum of Au_x/NP-TNTAs binary heterostructure is analogue to that of tenary counterpart, for both of which two chemical states of Au were observed, i.e., Au^+ and Au^0 (**Table S3**), verifying intrinsic core-shell nano-architecture of Au_x clusters.

Table S3. Binding energy *vs* chemical bond species for Au_x/NP-TNTAs binary heterostructure.

Element	***Au_x/NP-TNTAs (eV)***	***Chemical Bond Species***
Ti $2p_{3/2}$	458.41	Ti-O
Ti $2p_{1/2}$	464.12	Ti-O
O 1s A	529.60	Lattice oxygen (Ti-O)
O 1s B	531.48	Surface hydroxyl (Ti-OH)
Au $4f_{7/2}$ A	83.94	Metallic Au^0
Au $4f_{7/2}$ B	84.60	Au^+
Au $4f_{5/2}$ C	87.70	Metallic Au^0
Au $4f_{5/2}$ D	88.54	Au^+

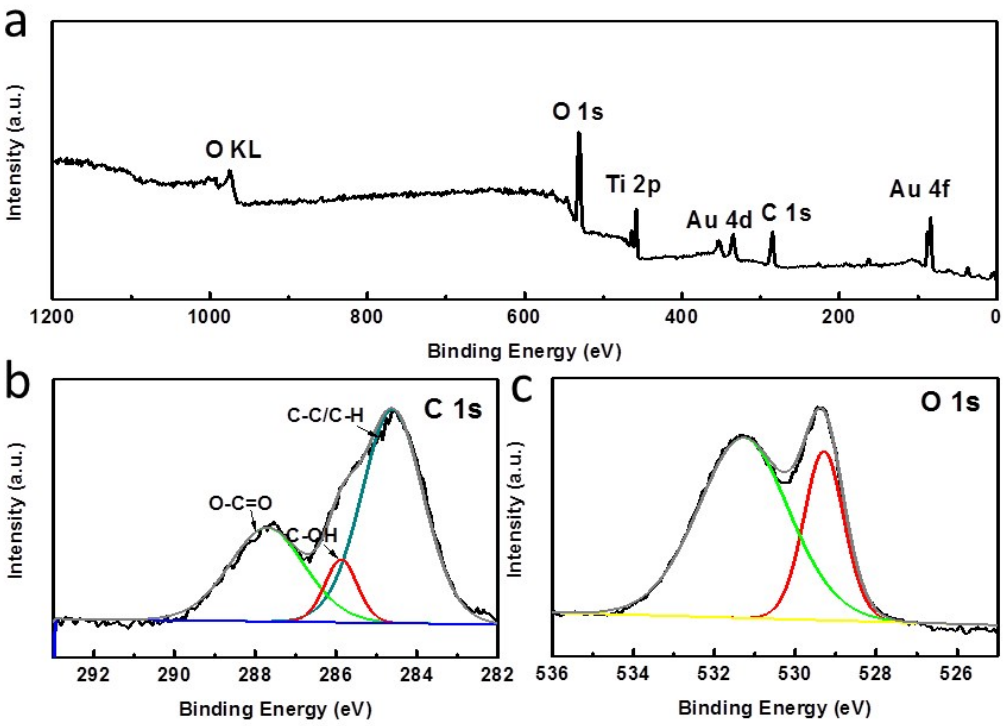

Fig. S11 (a) Survey spectrum and high-resolution XPS spectra of (b) C1s and (c) O 1s for Au_x/GQDs/ NP-TNTAs ternary heterostructure.

Table S4. Binding energy *vs* chemical bond species for Au_x/GQDs/ NP-TNTAs ternary heterostructure.

Element	***Au_x/NP-TNTAs (eV)***	***Chemical Bond Species***
Ti $2p_{3/2}$	458.19	Ti-O
Ti $2p_{1/2}$	463.92	Ti-O
O 1s A	529.30	Lattice oxygen (Ti-O)
O 1s B	531.27	Surface hydroxyl (Ti-OH)
C 1s A	284.60	C-C/C-H
C 1s B	285.88	C-OH/C-O-C
C 1s C	287.69	O-C=O
Au $4f_{7/2}$ A	83.75	Metallic Au^0
Au $4f_{7/2}$ B	84.57	Au^+
Au $4f_{5/2}$ C	87.53	Metallic Au^0
Au $4f_{5/2}$ D	88.41	Au^+

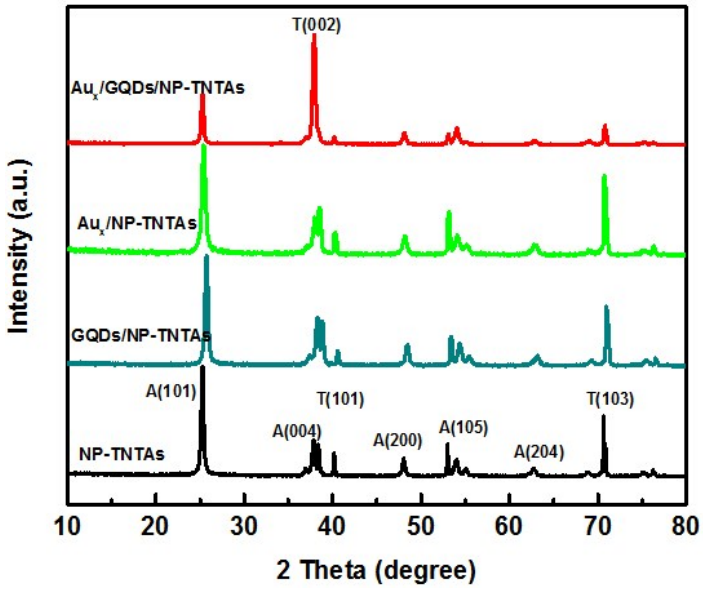

Fig. S12 XRD patterns of pristine NP-TNTAs, GQDs/NP-TNTAs, Au_x/NP-TNTAs binary and Au_x/GQDs/NP-TNTAs ternary heterostructures.

Note: No diffraction peaks corresponding to GQDs and Au_x clusters were observed in the XRD results, which can be ascribed to their low loading amount or probably their peaks were shield by the substantial TiO_2 peaks.

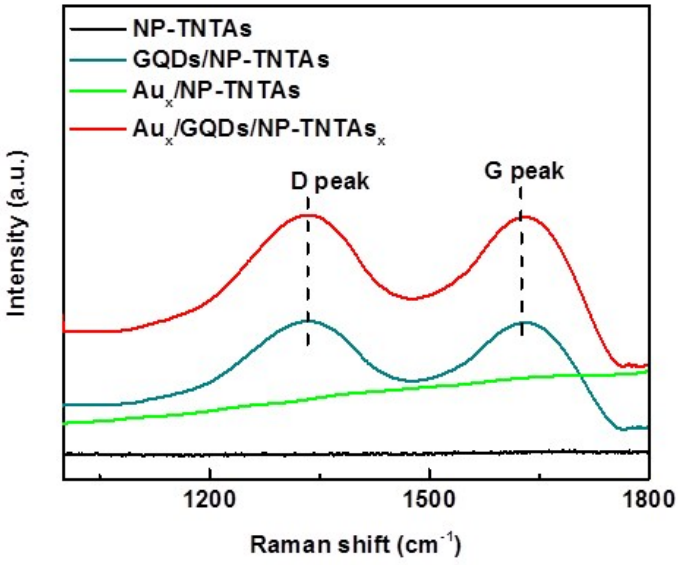

Fig. S13 Enlarged Raman spectra of pristine NP-TNTAs, GQDs/NP-TNTAs, Au_x/NP-TNTAs binary and Au_x/GQDs/NP-TNTAs ternary heterostructures.

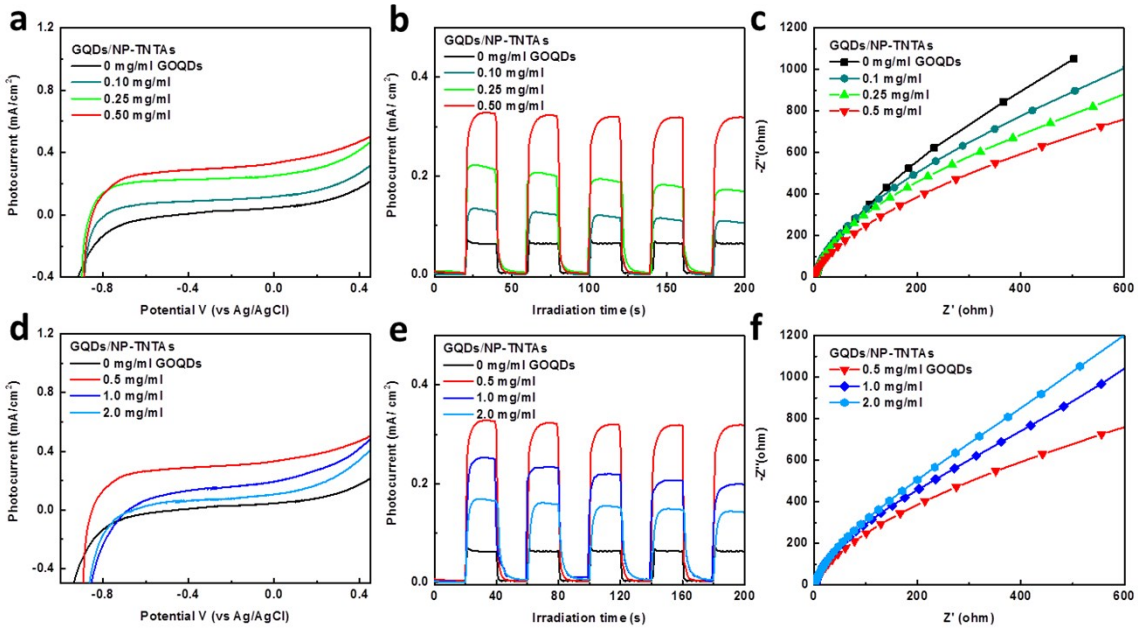

Fig. S14 (a & d) LSV, (b & e) on-off transient photocurrent response and (c & f) EIS results of GQDs/NP-TNTAs binary heterostructure prepared by dipping NP-TNTAs substrate into GOQDs aqueous solution with different concentration (i.e., 0, 0.10, 0.25, 0.50, 1.0 and 2.0 mg/mL) for 24 h. The PEC measurements were performed under simulated solar light irradiation (AM1.5, 100 mW/cm^2, 0.5 M Na_2SO_4, pH=5.8). The-obtained GOQDs/NP-TNTAs was calcined at 400 ºC in Ar for 1 h to promote the reduction of GOQDs to GQDs in fabricating GQDs/NP-TNTAs.

Note: It is apparent that GQDs loading amount exerts pronounced influence on the PEC water splitting performances of GQDs/NP-TNTAs binary heterostructure. Based on the above systematic investigation, optimal GOQDs concentration used for assembly on the NP-TNTAs framework is 0.5 mg/mL.

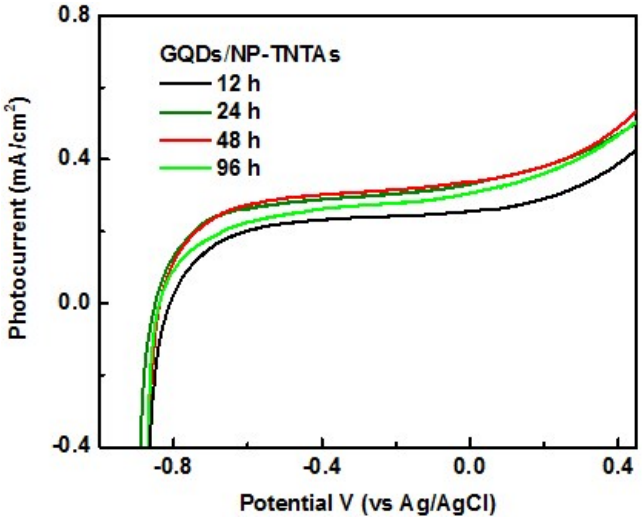

Fig. S15 LSV results of GQDs/NP-TNTAs binary heterostructure prepared by dipping NP-TNTAs substrate into GOQDs aqueous solution (0.5 mg/mL) with different dipping time (i.e., 12, 24, 48 and 96 h). The PEC measurements were performed under simulated solar light irradiation (AM1.5, 100 mW/cm^2, 0.5 M Na_2SO_4, pH=5.8).

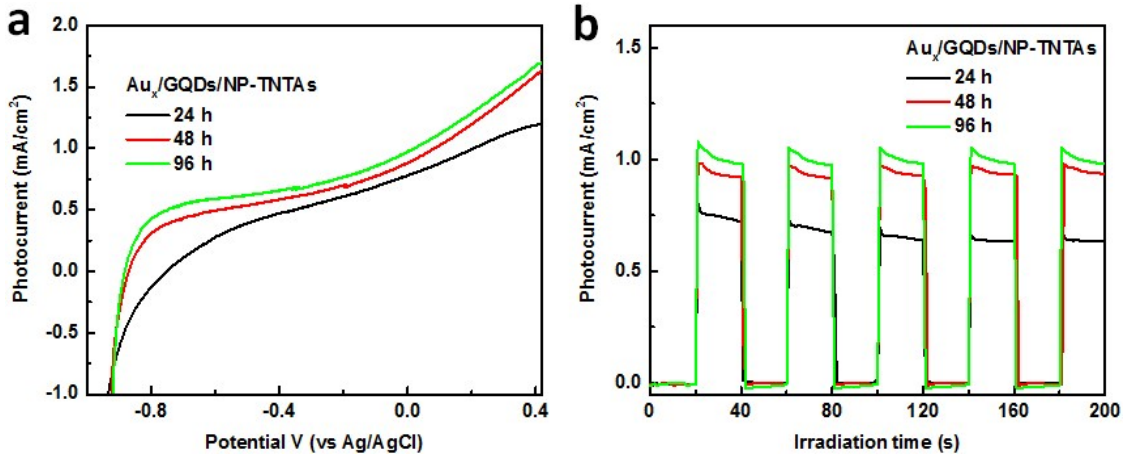

Fig. S16 (a) LSV and (b) on-off transient photocurrent responses of Au_x/GQDs/NP-TNTAs ternary heterostructure prepared by dipping GQDs/NP-TNTAs into Au_x clusters aqueous solution with different dipping time (i.e., 24, 48 and 96 h, GOQDs: 0.5 mg/mL). The PEC measurements were performed under simulated solar light irradiation (AM1.5, 100 mW/cm^2, 0.5 M Na_2SO_4, pH=5.8).

Note: Dipping time of GQDs/NP-TNTAs into Au_x clusters aqueous solution also exerts pronounced influence on the PEC water splitting performances of ternary heterostructure. The longer dipping time indicates the more deposition amount of Au_x clusters on the substrate. Obviously, optimal dipping time of GQDs/NP-TNTAs in the Au_x clusters aqueous solution is determined to be 96 h.

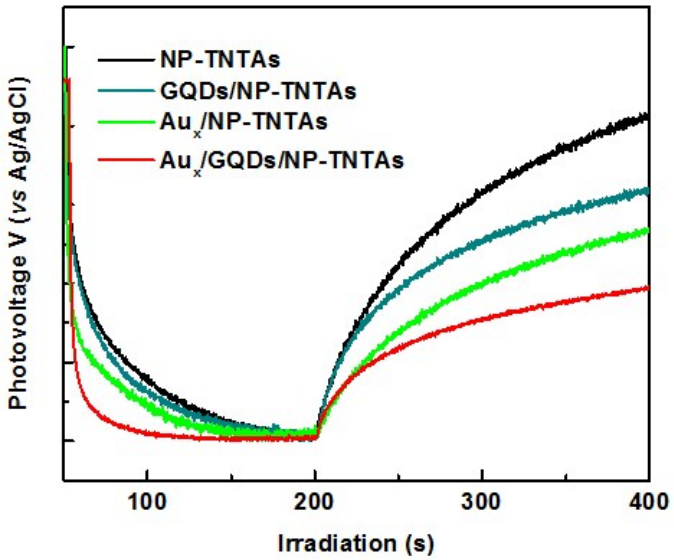

Fig. S17 Decay of open-circuit potential of pristine NP-TNTAs, GQDs/NP-TNTAs (GOQDs: 0.5 mg/mL, 48 h), Au_x/NP-TNTAs (Au_x: 96 h) binary and Au_x/GQDs/NP-TNTAs (GOQDs: 0.5 mg/mL, 48 h; Au_x: 96 h) ternary heterostructure upon turning off the light irradiation. The PEC measurements were performed under simulated solar light irradiation (AM1.5, 100 mW/cm^2, 0.5 M Na_2SO_4, pH=5.8).

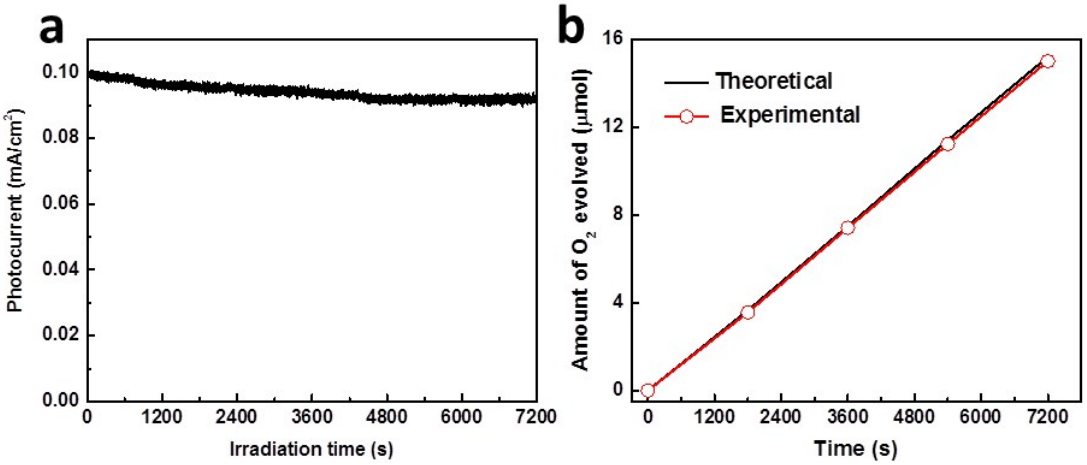

Fig. S18 (a) Photocurrent of Au_x/GQDs/NP-TNTAs ternary heterostructures under continuous simulated solar light irradiation with a bias of 0V vs. Ag/AgCl (AM1.5, 100 mW/cm^2) under simulated solar light irradiation (AM1.5, 100 mW/cm^2, 0.5 M Na_2SO_4, pH=5.8). (b) Comparison of oxygen evolution amount with theoretical result calculated based on the amount of consumed charges.

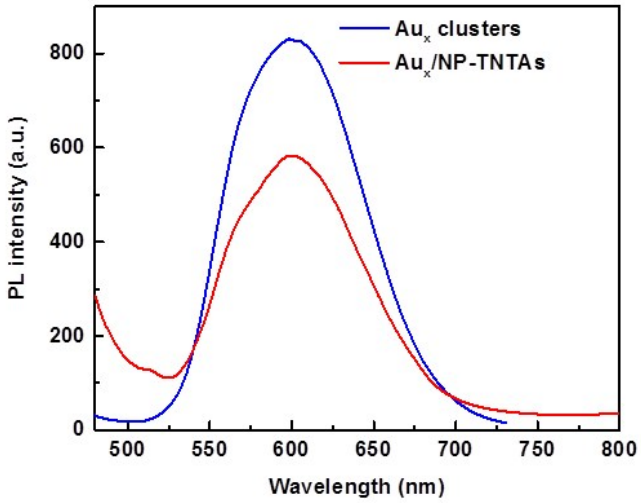

Fig. S19 PL spectra of Au_x clusters with addition of TiO_2 scratched from NP-TNTAs substrate with an excitation wavelength of 425 nm.

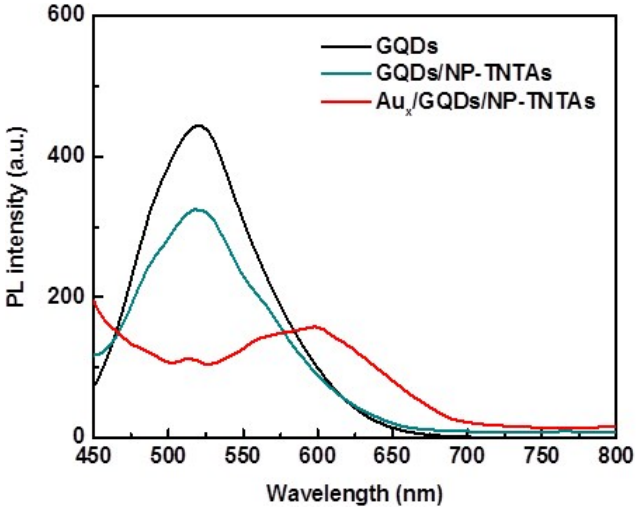

Fig. S20 PL results of GQDs with addition of TiO_2 scratched from NP-TNTAs substrate and Au_x/GQDs/NP-TNTAs with an excitation wavelength of 425 nm.

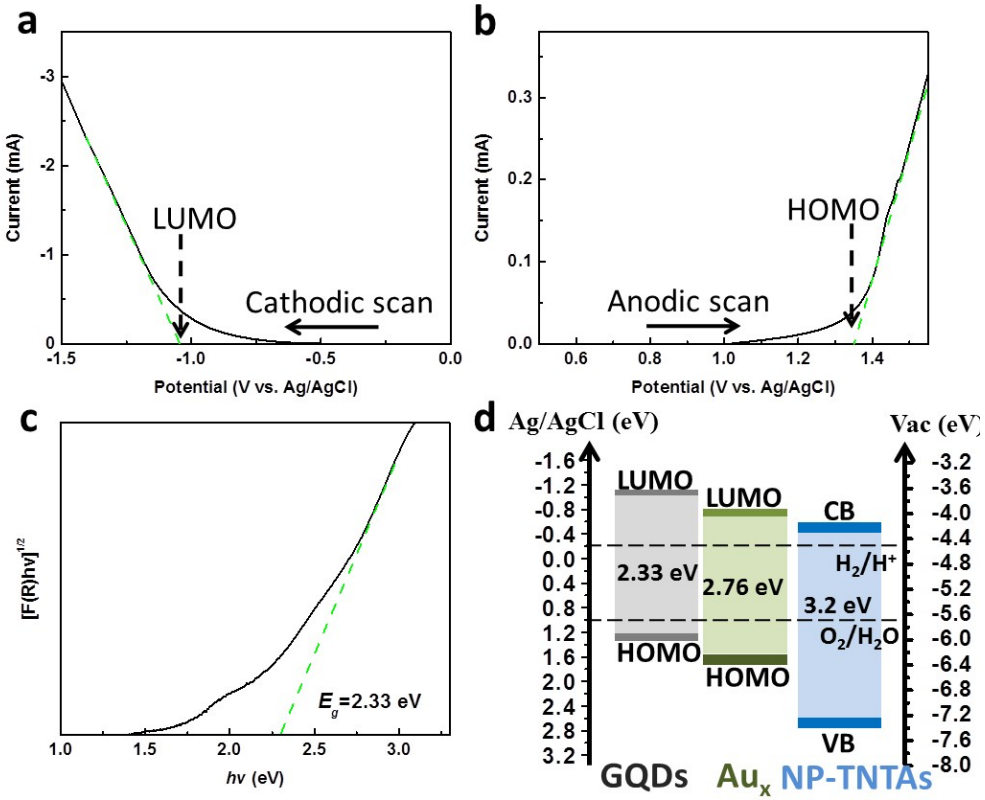

Fig. S21 (a) LUMO and (b) HUMO energy levels of GQDs determined by a cathodic scan (5 mV/s), energy and an anodic scan (5 mV/s), (c) plots of transformed Kubelka-Munk function *vs.* energy of light for GQDs, and (d) schematic illustration of the energy levels of GQDs, Au_x and NP-TNTAs substrate.

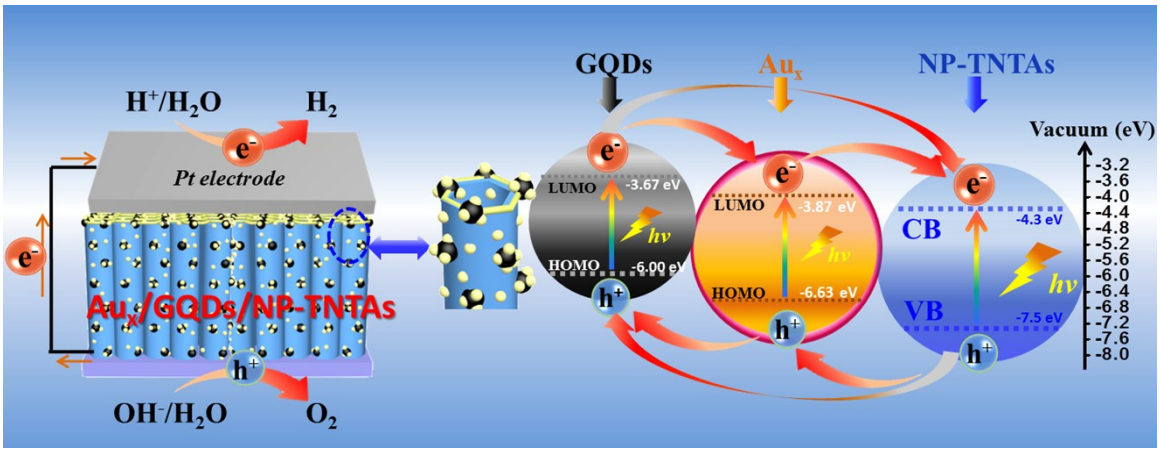

Fig. S22 Schematic illustration of the PEC water splitting mechanism of Au_x/GQDs/NP-TNTAs ternary heterostructure under simulated solar light irradiation.